



HAL
open science

Normalized kinetic energy as a hydrodynamical global quantity for inhomogeneous anisotropic turbulence

Pierre-Philippe Cortet, Pantxo Diribarne, Romain Monchaux, Arnaud Chiffaudel, François Daviaud, Bérengère Dubrulle

► **To cite this version:**

Pierre-Philippe Cortet, Pantxo Diribarne, Romain Monchaux, Arnaud Chiffaudel, François Daviaud, et al.. Normalized kinetic energy as a hydrodynamical global quantity for inhomogeneous anisotropic turbulence. *Physics of Fluids*, 2009, 21 (2), pp.025104. 10.1063/1.3073745 . hal-01847323

HAL Id: hal-01847323

<https://ensta-paris.hal.science/hal-01847323v1>

Submitted on 23 Jul 2018

HAL is a multi-disciplinary open access archive for the deposit and dissemination of scientific research documents, whether they are published or not. The documents may come from teaching and research institutions in France or abroad, or from public or private research centers.

L'archive ouverte pluridisciplinaire **HAL**, est destinée au dépôt et à la diffusion de documents scientifiques de niveau recherche, publiés ou non, émanant des établissements d'enseignement et de recherche français ou étrangers, des laboratoires publics ou privés.

Normalized kinetic energy as a hydrodynamical global quantity for inhomogeneous anisotropic turbulence

Pierre-Philippe Cortet, Pantxo Diribarne, Romain Monchaux, Arnaud Chiffaudel, François Daviaud, and Bérengère Dubrulle^{a)}

Service de Physique de l'État Condensé, DSM, CEA Saclay, CNRS URA 2464, 91191 Gif-sur-Yvette, France

(Received 20 May 2008; accepted 13 December 2008; published online 23 February 2009)

We introduce a hydrodynamical global quantity δ that characterizes turbulent fluctuations in inhomogeneous anisotropic flows. This time dependent quantity is constructed as the ratio of the instantaneous kinetic energy of the flow to the kinetic energy of the time-averaged flow. Such a normalization based on the dynamics of the flow makes this quantity comparable from one turbulent flow to any other. We show that $\delta(t)$ provides a useful quantitative characterization of any turbulent flow through generally only two parameters, its time average $\bar{\delta}$ and its variance δ_2 . These two quantities present topological and thermodynamical properties since they are connected, respectively, to the distance between the instantaneous and the time-averaged flow and to the number of degrees of freedom of the flow. Properties of $\bar{\delta}$ and δ_2 are experimentally studied in the typical case of the von Kármán flow and used to characterize the scale by scale energy budget as a function of the forcing mode as well as the transition between two flow topologies. © 2009 American Institute of Physics. [DOI: 10.1063/1.3073745]

I. INTRODUCTION

Turbulent flows are characterized by a very large number of degrees of freedom. High spatial resolutions are therefore useful to investigate turbulence in numerics or experiments. Nowadays, direct numerical simulations routinely deal with three-dimensional vector fields spanning over a 1024^3 array of grid points. Standard particle image velocimetry (PIV) measurements of experimental flow provide instantaneous snapshots of the velocity field over 64^2 – 128^2 arrays. The challenge is therefore not anymore to visualize the flow, but rather to analyze and condense the huge amount of information present in a turbulent flow. In classical homogeneous, isotropic turbulence, this challenge is milder since single point measurements such as velocity increments or turbulence intensity already provide a representative and yet affordable piece of information.¹ In nonhomogeneous, nonisotropic flows, the challenge is still open. Different strategies have been used in the past, depending on the available information: in numerical flows, where all the information about the flow is accessible, priority has often been given to global quantities, built through spatial averaging of physically relevant quantities such as the energy, helicity, and enstrophy.² In experiments, the possibilities have long been restricted to local, single point measurements,^{3,4} or to nonhydrodynamical global quantities such as injected power.^{5–8} The recent advent of PIV measurements has changed the challenge for experimental flows. The problem is now to develop the relevant tools enabling the description of turbulence from hydrodynamical quantities with as few degrees of freedom as possible. Successful candidates should ideally enable classifications of turbulent flows. In the absence of systematic theories of turbulence, such as a thermodynamics (that would

distinguish between, e.g., “hot” and “cold” turbulence^{9–12}) or a topological theory,^{13,14} one is left with empirical tools.

In this article, we present such an empirical tool, $\delta(t)$, defined as a normalized kinetic energy of the flow that enables characterization of flows with nonzero time average. First, we introduce and discuss in Sec. II the global time dependent quantity $\delta(t)$. In Sec. III, we present our experimental setup and show how to compute practically $\delta(t)$ from stereoscopic particle image velocimetry (SPIV) measurements. In Sec. IV, we first show that $\delta(t)$ provides a useful quantitative characterization of turbulent flows through generally only two parameters, its time average $\bar{\delta}$ and its variance δ_2 , that quantify, respectively, the level of fluctuations compared to the mean flow and their ability to disturb the mean flow. These two quantities are introduced as a generalization of the classical local turbulence intensity i . Finally, we discuss applications of these new global measures of turbulence intensity. In particular, we show how these parameters may be used to study the influence of the forcing conditions on the flow, and even trace back to critical behaviors near bifurcations of the mean flow structure.

II. NORMALIZED KINETIC ENERGY AS A GENERALIZATION OF THE TURBULENCE INTENSITY

A. Turbulence intensity

The classical theory of homogeneous isotropic turbulence applies to flows with zero velocity average so that all the turbulence properties are contained in the temporal velocity fluctuations.¹ Real turbulent flows, with nontrivial boundary conditions and external forcing, often possess a nonzero mean flow that may or may not be stationary. In most of the early experimental works about turbulence, this nonzero mean flow is used to transform “local” temporal

^{a)}Electronic mail: berengere.dubrulle@cea.fr.

information into “extended” spatial information through the so-called Taylor hypothesis. Actually, velocity measurements were performed through hot wire probes providing temporal variations of the velocity at fixed points. A natural parameter quantifying the intensity of turbulence has therefore been introduced as

$$i = \sqrt{\frac{\overline{V^2} - \bar{V}^2}{\bar{V}^2}},$$

where V is the velocity and \bar{X} refers to the time average of variable X . While such a parameter clearly characterizes fluctuations in a homogeneous flow, one may question its relevance in more general anisotropic inhomogeneous flows where turbulence intensity depends on the measurement point [cf. Figs. 1(a) and 1(d)]. For example, i diverges around stagnation points or shears so that no robust global quantity can be built by integrating or averaging i over the whole flow. An illustration of the importance of that issue may be given in the typical inhomogeneous anisotropic case of the von Kármán flow. This flow, generated in between two counter-rotating coaxial impellers, has received a lot of interest^{15–19} as a simple way to obtain experimentally a very large Reynolds number flow in a compact design ($\text{Re} \sim 10^6$ in a table top water apparatus). In the equatorial shear layer of such a flow, fluctuations are large and exhibit similar local properties as in large Reynolds number experimental facilities devoted to homogeneous turbulence.^{4,16,20,21} Away from the shear layer, one observes a decrease in the turbulence intensity,^{22,23} as seen in Figs. 1(a) and 1(d). Overall, the flow is strongly turbulent so that the instantaneous velocity fields, measured by means of a PIV system, strongly differ in a nontrivial manner from their time average [cf. Figs. 1(b) and 1(c)]. To overcome these limitations, we introduce a normalized kinetic energy in order to find a global generalization of the turbulence intensity.

B. Normalized kinetic energy

The kinetic energy E of a turbulent flow is a conserved quantity in the inviscid force-free limit. This observation is at the heart of the description of turbulence through an energy cascade from large to small scales even if in real stationary turbulent flows, kinetic energy $E(t)$ is only conserved in average. This quantity therefore appears as a natural global observable to study turbulence. However, without proper normalization, E does depend on the Reynolds number or on the forcing conditions (vessel shape, injection device,...). In numerical simulations, the kinetic energy is therefore classically normalized using the typical velocity which appears in the Reynolds number definition. In the sequel, we rather adopt a global normalization, through the kinetic energy of the time-averaged flow, to define our normalized global kinetic energy

$$\delta(t) = \frac{E(t)}{\bar{E}}. \quad (1)$$

This normalization finds its relevance in the fact it is based on the whole velocity field of the flow and not only on the

forcing amplitude. The kinetic energy of the flow can be classically computed from the velocity field $V(\vec{x}, t) = [u(\vec{x}, t), v(\vec{x}, t), w(\vec{x}, t)]$ as a spatial average $E(V(t)) = \langle V^2(t) \rangle$. δ can therefore be recast as

$$\delta(t) = \frac{\langle V^2(t) \rangle}{\langle \bar{V}^2 \rangle},$$

where $\langle X \rangle$ and \bar{X} refer, respectively, to spatial and time average of X , and $V(\vec{x}, t)^2 = u^2 + v^2 + w^2$ is the local kinetic energy density at time t .

Note that this scalar parameter is time dependent and generally widely fluctuates in time (cf. Fig. 2). We then define two time independent parameters, $\bar{\delta}$ and δ_2 , that are the time average and variance of $\delta(t)$, respectively, as

$$\bar{\delta} = \overline{\langle V^2(t) \rangle} / \langle \bar{V}^2 \rangle,$$

$$\delta_2 = \sqrt{\overline{\delta(t)^2} - \bar{\delta}^2}.$$

We show in Sec. III that these two quantities fully characterize $\delta(t)$ provided that the considered time series of sampled fields are uncorrelated.

To our knowledge, these quantities have never been studied in the analysis of experimental or numerical turbulent flows except within the framework of dynamo theory.²⁴ They have however several built-in thermodynamic and topological characteristics that make them suitable for a classification of turbulent flows. First, in a homogeneous turbulent flow, $\bar{\delta} = i^2 + 1$, so that $\bar{\delta}$ is a global generalization of the local turbulence intensity i . Additionally,

$$(\bar{\delta} - 1) \langle \bar{V}^2 \rangle = \overline{\langle (V - \bar{V})^2 \rangle} = \frac{1}{\mathcal{V}} \int_{\mathcal{V}} d^3\vec{x} (V - \bar{V})^2,$$

where the sum runs over the volume \mathcal{V} of the flow. The quantity under the overline is nothing but the square of the mean distance (using norm 2) between the instantaneous flow and the mean flow in the functional space. Therefore, the quantity $(\bar{\delta} - 1)$ is a global measure of how far, on average, the instantaneous velocity field is from its time average. If $\bar{\delta}$ is close to one, one therefore expects the instantaneous flow to strongly resemble the mean flow. If $\bar{\delta}$ is much greater than 1, the instantaneous field will be more remote from the mean flow. This interpretation of $\bar{\delta}$ is used in the Appendix to draw a rough study of the convergence of the von Kármán flow toward its time average.

Second, δ_2 appears as a parameter that has already been studied if it is rewritten as

$$\delta_2 = \frac{\sqrt{\overline{E^2} - \bar{E}^2}}{\bar{E}} = \frac{E_{\text{rms}}}{\bar{E}}.$$

Indeed, as discussed in Ref. 25, this quantity varies in usual equilibrium systems like $1/\sqrt{N}$, where N is the number of degrees of freedom of the system. In dissipative forced flows, Aumaître *et al.*^{25,26} showed that it might be interpreted

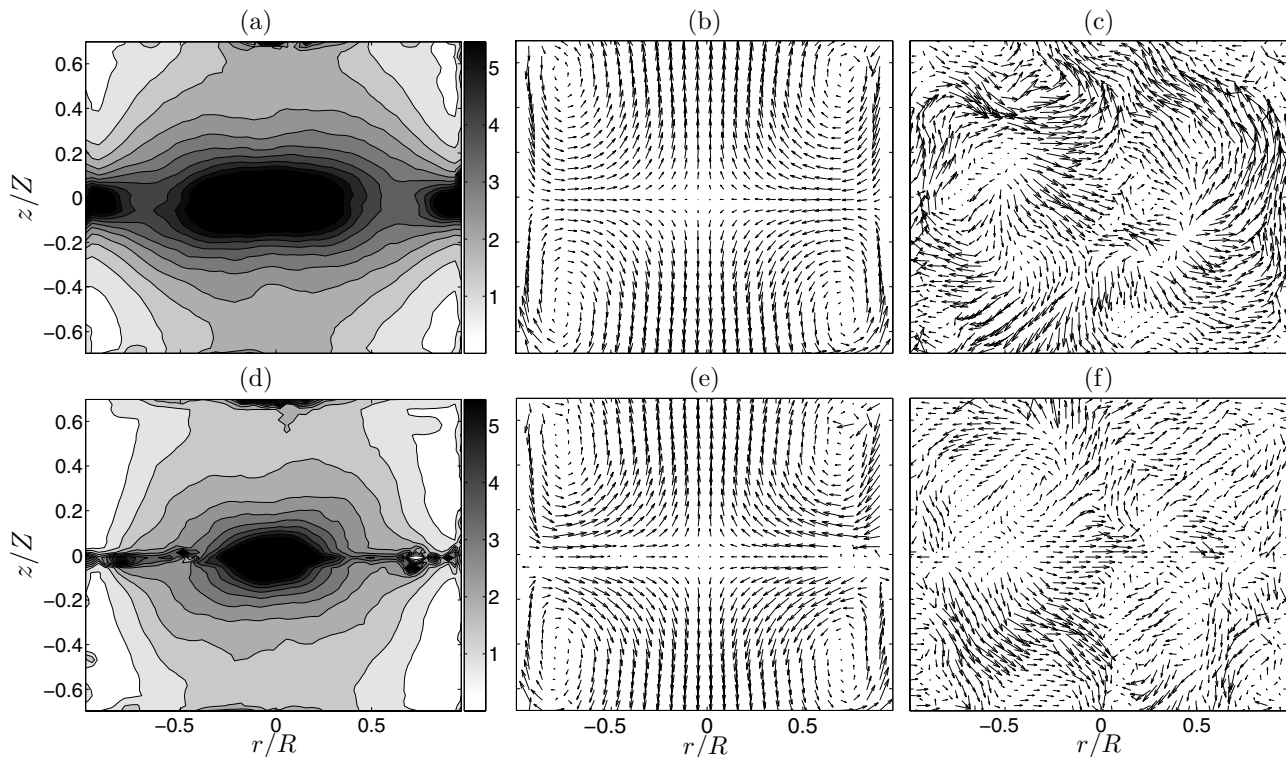


FIG. 1. [(a) and (d)] Maps of turbulence intensity i , [(b) and (e)] corresponding time-averaged, and [(c) and (f)] typical instantaneous velocity fields for two von Kármán flows [(a)–(c) and (d)–(f)] at the same Reynolds number but with slightly different geometry. Both flows correspond to the same experimental setup—TM60(+)—except for a narrow annulus inserted in the median plane of the flow in (d)–(f). In (a) and (d), for better visibility, the gray scale has been saturated at $i=6$ since values up to $i\sim 10^4$ can be reached in the median plane due to weak mean velocities and large fluctuations. Additionally, vectors of the instantaneous velocities have been scaled by half with respect to the mean field vectors.

as a measure of the effective degrees of freedom of the system. δ_2 therefore includes a thermodynamical information which will be proven useful in the sequel.

III. EXPERIMENTAL SETUP AND DATA PROCESSING

A. The von Kármán flow

1. Experimental setup

In order to illustrate and apply these concepts, we have worked with a specific axisymmetric turbulent flow: the von Kármán flow generated by two counter-rotating impellers in a cylindrical vessel. The cylinder radius and height are $R = 100$ and 240 mm, respectively. We have used two sets of impellers named TM60 and TM73.²⁷ These two models are flat disks of respective diameters 185 and 150 mm fitted with radial blades of height 20 mm and respective curvature radii 50 and 92.5 mm. The inner faces of the disks are $H = 180$ mm apart.

Impellers are driven by two independent motors rotating up to typically 10 Hz. More details about the experimental setup can be found in Ref. 28. The motor frequencies can be either set equal to get exact counter-rotating regime, or set to different values $f_1 \neq f_2$. We define two forcing conditions associated with the concave (convex) face of the blades going forward, denoted in the sequel by sense (–) [(+)]. We also work with two different vessel geometries, allowing the optional insertion of an annulus—thickness 5 mm, inner diameter 170 mm—in the equatorial plane. Both the forcing

condition and the annulus insertion strongly influence the level of fluctuation in the flow, thereby allowing to test experimentally the sensitivity and the relevance of $\delta(t)$, $\bar{\delta}$, and δ_2 . The working fluid is water.

2. Control parameters

From the two motor frequencies, f_1 and f_2 , we define two control parameters: a Reynolds number, Re , and a rotation number, θ . For the experiments described in this paper, the Reynolds number,

$$Re = \pi(f_1 + f_2)R^2\nu^{-1},$$

where ν is the fluid kinematic viscosity, ranges from

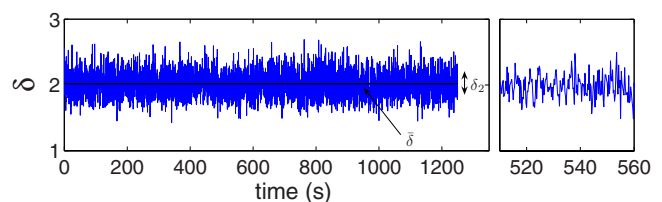


FIG. 2. (Color online) Example of the temporal evolution of $\delta(t)$ at two time scales: a full record of about 20 min on the left, and a focus on a 40 s sample on the right. A schematic illustration of the meaning of $\bar{\delta}$ and δ_2 is also provided over the longest time record.

1.25×10^5 to 5×10^5 so that the turbulence can be considered fully developed. The rotation number,

$$\theta = \frac{f_1 - f_2}{f_1 + f_2},$$

measures the relative influence of global rotation over a typical turbulent shear frequency. Indeed, the exact counter-rotating regime corresponds to $\theta=0$ and, for a nonzero rotation number, our experimental system is similar, within lateral boundaries, to an exact counter-rotating experiment at frequency $f=(f_1+f_2)/2$, with an overall global rotation at frequency $(f_1-f_2)/2$.^{18,22} In our experiments, we vary θ from -1 to $+1$, exploring a regime of relatively weak rotation-to-shear ratio.

3. Mean flow topology

In the exact counter-rotating regime, i.e., for $\theta=0$, the standard mean flow is divided into two toric recirculation cells separated by an azimuthal shear layer [cf. Figs. 1(b) and 1(e)]. As θ is driven away from zero, a change in topology occurs at a critical value θ_c : The mean flow bifurcates from the two counter-rotating recirculation cells to a single cell.¹⁸ θ_c depends on the forcing and the geometry. For example, in the configuration with TM73 impellers, rotation sense (+) and the annulus, we measure $\theta_c=0.17 \pm 0.01$ through torque measurements. In the case TM60(−), this turbulent bifurcation becomes highly singular and gives rise to multistability between the two turbulent flow symmetries, O(2)–SO(2).^{18,29}

B. Measurements and data processing

Measurements are done with a SPIV system. The SPIV data provide the radial, axial, and azimuthal velocity components on a 95×66 point grid covering a whole meridian plane of the flow through a time series of about 5000 regularly sampled values, for experiments at $\theta=0$. The series of data with a varying rotation number θ are acquired with a smaller statistics of 600 samples. The sampling frequency is set between 1 and 4 Hz, corresponding to one sample record every 1–10 impeller rotations. The total acquisition time is about ten minutes, i.e., one order of magnitude longer than the characteristic time of the slowest patterns of the turbulent flow. Fast scales are statistically sampled.

The velocity fields are nondimensionalized using a typical velocity $V_0=2\pi R(f_1+f_2)/2$ based on the radius of the cylinder and the rotation frequencies of the impellers. The resulting velocity fields are windowed so as to fit to the boundaries of the flow and remove spurious velocities measured in the impellers and the boundaries. The resulting fields consist of 58×58 point velocity maps. Two types of filtering are further applied to clean the data: first, a global filter to get rid of all velocities larger than $3 \times V_0$; then, a local filter (based on velocities of nearest neighbors) to remove isolated spurious vectors. Typically, 1% of the data are changed by this processing.

C. Data analysis

From a practical point of view, we use two different methods to compute $\delta(t)$ from our PIV measurements. In the direct method, we compute δ by spatially averaging the kinetic energy density of instantaneous and time-averaged flows. Since we measure the full velocity field in a single meridian plane only, we cannot compute true three-dimensional (3D) spatial averages. Practically, we estimate the 3D spatial average of any quantity X assuming its axisymmetry such as

$$\langle X(r, z) \rangle = \frac{1}{R^2 H} \int_{-R}^R |r| dr \int_{-H/2}^{H/2} dz X(r, z).$$

For time-averaged quantities, the statistical axisymmetry of the von Kármán flow justifies this procedure. For instantaneous quantities $X(r, z, t)$, this is not the case. Therefore, our estimation of $\delta(t)$ may be slightly flawed. However, time averaging and spatial averaging over the angular variable θ , i.e., over the different meridian planes, are equivalent operations since spatial structures of the flow in the θ direction are rotating. Such “ergodicity” makes our estimation of $\bar{\delta}$ correct. Since velocity fields are discrete in space and time, spatial integration is done with a classical numerical trapezoid summation method whereas time integration is performed through simple summation.

The parameter δ can also be obtained by a spectral method. For this, we compute the spatial power spectral density (PSD) of the discrete velocity fields as

$$\tilde{E}(k_r, k_z, t) = \tilde{W} \tilde{W}^*,$$

where $\tilde{W} = \tilde{W}(k_r, k_z, t)$ is the two-dimensional spatial Fourier transform of $W(r, z, t) = \sqrt{|r|} V(r, z, t)$ and \tilde{W}^* its complex conjugate. Then, we compute δ using Parseval’s identity

$$\int \int |r| dr dz V^2 = \int \int dk_r dk_z \tilde{W} \tilde{W}^*$$

and get

$$\delta(t) = \frac{\int \int dk_r dk_z \tilde{E}(k, t)}{\int \int dk_r dk_z \tilde{E}_0(k)}, \quad (2)$$

where \tilde{E}_0 is the PSD of the time-averaged flow

$$\tilde{E}_0(k_r, k_z, t) = \tilde{W} \tilde{W}^*.$$

IV. RESULTS AND APPLICATIONS

A. Basic properties of δ

1. Statistical properties

As discussed in Sec. II, $\delta(t)$ widely fluctuates in time. However, its statistical properties in the exact counter-rotating case are rather simple since its probability density function (PDF) is nearly Gaussian as illustrated in Fig. 3(a). Actually, this property holds at different Reynolds numbers [cf. Fig. 3(a)] and for all forcing and geometry conditions studied in the present paper [cf. Fig. 3(b)]. A striking feature is that global rotation does not change the statistical proper-

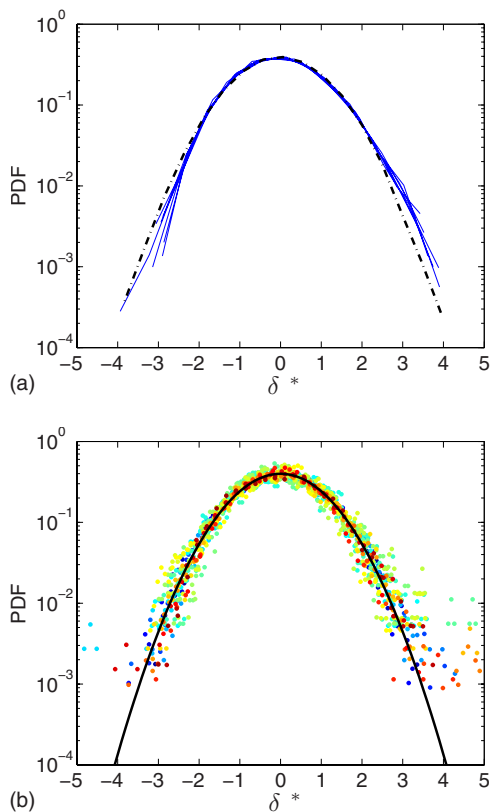


FIG. 3. (Color online) Centered and reduced PDF of $\delta(t)$, (a) for the TM73(-) configuration with annulus at $\theta=0$ and for seven different Reynolds numbers ranging from 1.25×10^5 to 5×10^5 (5000 samples), and (b) for the TM73(+) configuration without annulus for 16 experiments performed with different values of rotation number $\theta=(f_1-f_2)/(f_1+f_2)$ ranging from 0 to 1 (600 samples). $\delta^*=(\delta-\bar{\delta})/\delta_2$ is the centered reduced value of δ . The dashed-dotted lines are Gaussian functions of zero mean and unit variance. Data of (b) are more scattered than those of (a) because of the difference in statistics.

ties of the flow since the PDFs are nearly Gaussian at any θ . Consequently, we can describe and fully characterize the total energy temporal distribution using only the two scalar parameters $\bar{\delta}$ and δ_2 .

Finally, we have to notice that the nearly Gaussian PDFs of δ present however a small asymmetry with high δ values in excess [at least in Fig. 3(a)]. We may highlight the resemblance between this asymmetry and the one observed in the PDFs of injected power in a closed turbulent flow, which is of the same order of magnitude as ours in Refs. 7 and 8 and much larger in Refs. 5 and 6. However, the theoretical link between kinetic energy and injected power is controversial^{30,31} so that no safe analogy can be drawn.

2. Dependence on the Reynolds number

For a given forcing, i.e., for a given impeller shape and a given rotation sense, we observe a very weak dependence of $\bar{\delta}$ with Re in the studied range as one can see in Fig. 4. The largest dispersions, of the order of 8%, are observed in the negative-rotation sense for both TM60 and TM73 impellers without annulus. For any other forcing condition, the dispersion is less than 5%. Similar conclusions hold for δ_2 represented in Fig. 4 using error bars. This behavior is not sur-

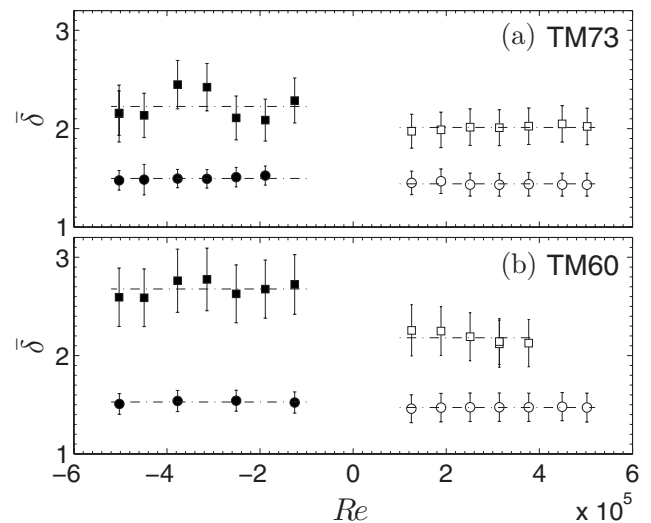


FIG. 4. $\bar{\delta}$ as a function of Reynolds number Re for $\theta=0$. Negative Re corresponds to rotation sense (-). (a) and (b) correspond, respectively, to TM73 and TM60 impellers, with (\circ) and without (\square) annulus. Dashed-dotted lines correspond to the mean value of $\bar{\delta}$ for each configuration and δ_2 is represented using error bars.

prising since in our water experiments the Reynolds number is so large that we are in the fully developed turbulent regime where statistical properties have already been shown not to depend on the Reynolds number.^{29,32,33} On the contrary, we expect a different behavior when lowering the Reynolds number³² since in the limit of very low Re , the instantaneous flow is laminar and identical to the mean flow: $\delta(t)=\bar{\delta}=1$. The study of the transition between laminar and fully turbulent regime requires the use of, e.g., glycerol-water mixing and is beyond the scope of the present paper. Note however that this transition has already been studied in the von Kármán experiment—TM60(-) without annulus at $\theta=0$ —by Ravelet *et al.*²⁹ using a one point measurement laser Doppler velocimetry system. It has been shown that the local value of the variance of the azimuthal velocity, $\overline{v_\theta^2}-\bar{v}_\theta^2$, behaves as $(Re-Re_c)^{1/2}$ and saturates above $Re_t=3300$, where $Re_c=330$ corresponds to the transition from steady to oscillatory laminar flow and Re_t to the onset of the fully turbulent inertial regime. A similar behavior is encountered in direct numerical simulations of the Taylor–Green flow,²⁴ where an increase in $\bar{\delta}$ from 1 at low Re to a saturation value of 3 for Re above 10^3 has been observed.

B. Influence of forcing and annulus

It is difficult to estimate turbulence intensity by simply looking at an instantaneous velocity field [cf. Figs. 1(c) and 1(f)]. To achieve this, the local turbulence intensity i maps [cf. Figs. 1(a) and 1(d)] constitutes a good qualitative tool to estimate the overall turbulence intensity and structure of the considered flow. However, a quantity like δ is needed to provide a global quantitative tool.

TABLE I. Values of $\bar{\delta}$ and δ_2 for various configurations.

Impellers	$\bar{\delta}$				δ_2			
	TM60		TM73		TM60		TM73	
Sense	(-)	(+)	(-)	(+)	(-)	(+)	(-)	(+)
Without annulus	2.64	2.18	2.22	2.02	0.30	0.24	0.24	0.18
With annulus	1.52	1.47	1.50	1.48	0.11	0.15	0.11	0.12

1. Effect of impeller and vessel geometry

As reported in Table I, the values of $\bar{\delta}$ and δ_2 allow to quantify the differences in the turbulence fluctuations level as a function of the forcing configurations (TM60 and TM73, with or without annulus). The major result of Table I is the effect of the annulus which systematically reduces $\bar{\delta}$ and δ_2 , meaning that the instantaneous flow is much closer to the mean flow. A great part of this drop probably reflects the reduction of the slow fluctuations of the shear layer already known from time spectral analysis to be responsible for a major part of the energy fluctuations.²⁹ From a spatial point of view, this reduction is the consequence of the expected locking of the shear layer in the annulus plane which appears in direct visualizations of the flow. Additionally, we note that the annulus tends to collapse all values of $\bar{\delta}$ to 1.5 ± 0.03 . In contrast, a dispersion of about thirty percents remains on the variance δ_2 .

2. Qualitative interpretation

To understand the measures presented in the last paragraph, we report visual observations of the flow seeded with bubbles [cf. Fig. 5]. Such visualizations allow to unveil spatial structures of turbulence and especially the largest patterns which exhibit the slowest time dynamics. Let us describe our observations in the TM73 impellers configuration.

Without annulus, the main structure of the free shear layer at very high Reynolds number consists of three big fluctuating vortices, i.e., a $m=3$ azimuthal wave number mode [cf. Figs. 5(a) and 6]. The size of these vortices is almost the full free height of the vessel for sense (-) and somewhat smaller for sense (+). These vortices fluctuate in azimuthal position as well as in amplitude or apparent size. Nucleation and merging frequently occur.

In the presence of an annulus, the azimuthal $m=3$ periodicity remains unchanged. However, the three vortex cores split into pairs of smaller corotating vortices attached to the leading edges of the annulus [see Fig. 5(b) and the schematic view in Fig. 6]. This splitting corresponds to the growth of an $m=6$ harmonics: the fundamental $m=3$ mode is impeded by the annulus and some of its energy is transferred to its first harmonics. The strong reduction in $\bar{\delta}$ and δ_2 is probably the trace of this scale change in the shear layer structure. We can note that within its thermodynamical interpretation given at the end of Sec. II, the decrease in δ_2 with increasing number of vortices in the shear layer may also be viewed as due to an increase in the number of degrees of freedom of the system in agreement with conclusions drawn in Ref. 8. Fur-

thermore, we observe the temporal dynamics of the shear layer vortices which is different for both senses of rotation. For sense (+), the vortices keep high mobility and fluctuation levels. On the contrary, for sense (-), the vortices are almost steady: merging, nucleation, and large azimuthal excursions are inhibited. The only remaining dynamics is an azimuthal vibration of their center at a frequency of a few hertz. This qualitative observation is corroborated by the behavior of δ_2 : even if $\bar{\delta} \sim 1.5$ in both cases, δ_2 is lower in the (-) senses, where the vortex pairs are more stable.

3. Scale by scale characterization

a. Spatial spectra. By construction, $\bar{\delta}$ accounts for the total fluctuating kinetic energy of the turbulent flow. The use of PSD as an intermediate step to compute $\bar{\delta}$ [cf. Eq. (2)] can provide useful information about the distribution of the energy over the various length scales of the flow, as illustrated in Figs. 7 and 8. Indeed, in Fig. 7, we compare the time-averaged PSD of the instantaneous velocity fields, $\bar{\tilde{E}}(k)$, to the PSD of the corresponding time-averaged field, $\tilde{E}_0(k)$, for the two TM73(+) setups, with and without annulus.

In the spirit of the definitions of turbulent intensity i and of the quantity δ , and because we do access the full spatial spectra, we choose to normalize the PSD by the total kinetic energy of the mean flow. Therefore, the integrals of the displayed curves for the two time-averaged flows are equal to 1. The wave number k is given by $k^2 = k_r^2 + k_z^2$.

In the time-averaged PSD of the instantaneous flow, the major part of the fluctuating kinetic energy is concentrated close to the forcing scale, where the energy is injected, like in any homogeneous and isotropic turbulent flow. On the contrary, at higher k , the slopes of the different PSDs are close to -2 and larger than the classical $-5/3$ exponent observed for homogeneous isotropic turbulence.

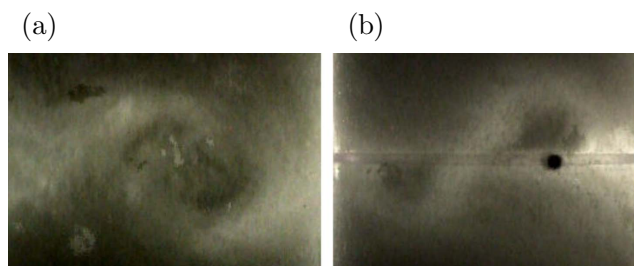


FIG. 5. (Color online) Visual observations of the von Kármán flow seeded with bubbles with TM73 impellers, (a) without annulus and (b) with annulus.

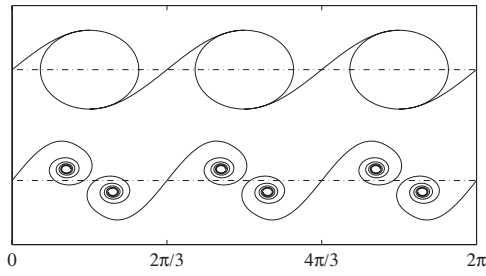


FIG. 6. Sketch of the shear layer patterns, on the developed cylinder (θ, z), from visual observations at high Reynolds number. Without annulus (top sketch), the shear produces a triplet of large corotating vortices, corresponding to a $m=3$ mode. In the presence of the equatorial annulus (bottom sketch), the pattern is still $m=3$ periodic but the three vortex cores split into corotating pairs: Some energy is transferred from the fundamental $m=3$ mode to its first $m=6$ harmonics.

b. Comparing instantaneous and time-averaged flows.

We observe in Fig. 7 that the kinetic energy spectra $E_0(k)$ of the time-averaged flow are below the average of the instantaneous spectra $\bar{E}(k)$ for all k . Their relative difference

$$\Delta\mathcal{E}(k) = \frac{\bar{E}(k) - \tilde{E}_0(k)}{\tilde{E}_0(k)}$$

measures the average relative excess of kinetic energy at wavenumber k in the instantaneous flow with respect to the corresponding amount of energy in the time-averaged flow. This quantity, which depends on the presence or the absence of the annulus, is evaluated in Table II. At low wavenumber, the relative excess of kinetic energy $\Delta\mathcal{E}(1/D)$ is 0.8 without annulus and only 0.2 with annulus, i.e., four times less and quite a small value. At higher wavenumber, $\Delta\mathcal{E}$ reaches a plateau close to 2 for both configurations. We conclude that when annulus is inserted, the instantaneous flow generally looks much closer to the time-averaged flow than without annulus, especially at large scale.

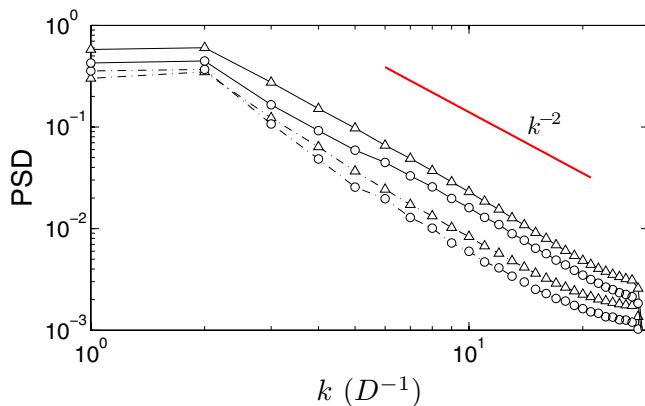


FIG. 7. (Color online) Two-dimensional time-averaged PSD of instantaneous flows $\bar{E}(k)$ (solid lines) and PSD of the corresponding time-averaged flows $\tilde{E}_0(k)$ (dashed-dotted lines) for two experiments performed with setup TM73(+), without the annulus (Δ) and with the annulus (\circ). The PSD are normalized by the total kinetic energy of the mean flow and wavenumbers are normalized by the PIV window size $D=1.93R$.

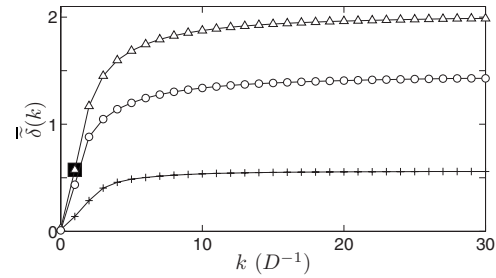


FIG. 8. $\bar{\delta}(k)$ as function of k for TM73(+) setups without (Δ) and with annulus (\circ). The specific data point $\bar{\delta}(1/D)$ is represented with a large black symbol (\blacksquare). The difference $\Delta\bar{\delta}(k)$ between the two curves is also displayed ($+$). At high k , this difference converges asymptotically to $\Delta\bar{\delta}$ and is of the order of $\bar{\delta}(1/D)$ without annulus (see text for details). Wavenumbers are normalized by the PIV window size $D=1.93R$.

c. *The annulus as a high-pass spatial filter.* To quantify more precisely the weight of each scale in $\delta(t)$, we introduce $\tilde{\delta}(k, t)$ defined as

$$\tilde{\delta}(k, t) = \frac{\int_0^k dk' \tilde{E}(k', t)}{\int_0^\infty dk' \tilde{E}_0(k')}$$

so that $\tilde{\delta}(k, t) \rightarrow \delta(t)$ when $k \rightarrow \infty$. In Fig. 8, $\bar{\delta}(k)$ is plotted for TM73(+) flows with and without annulus. These curves represent the integrals from 0 to k of the normalized PSD of Fig. 7. They converge toward $\bar{\delta}$ at large k , i.e., $\bar{\delta}(\infty) = \bar{\delta}$.

First of all, we see that the contribution of the five first wavenumbers, i.e., of spatial modes larger than $D/5 \approx R/10$, is about 80% of the total value of $\bar{\delta}$.

Additionally, in Fig. 8, we note that the fluctuation level in the first $k=1/D$ mode of the $\bar{\delta}(k)$ curve without annulus (the data point has been emphasized) and the difference $\Delta\bar{\delta}$ between the two flows—without (*w/o*) and with (*w*) annulus—are of the same order of magnitude,

$$\bar{\delta}_{w/o}(1/D) \approx \bar{\delta}_{w/o} - \bar{\delta}_w = \Delta\bar{\delta}.$$

This has also been verified for the three other couples of flows. The effect of the annulus may thus be seen as a high-pass spatial filter, filtering the largest patterns of the flow, which confirms the sketch presented in Fig. 6. Finally, the quantity $\tilde{\delta}(k, t)$ appears as an efficient tool to track the spectral changes in turbulent scales.

TABLE II. $\Delta\mathcal{E}(k)$ measures the average relative excess of kinetic energy at wavenumber k in the instantaneous flow with respect to the corresponding amount of energy in the time-averaged flow. It is evaluated from the spectra at low ($1/D$) and at higher (between $5/D$ and $10/D$) wavenumbers where a plateau is observed.

k	$1/D$	$5/D-10/D$
Without annulus	0.8	2.3
With annulus	0.2	1.7

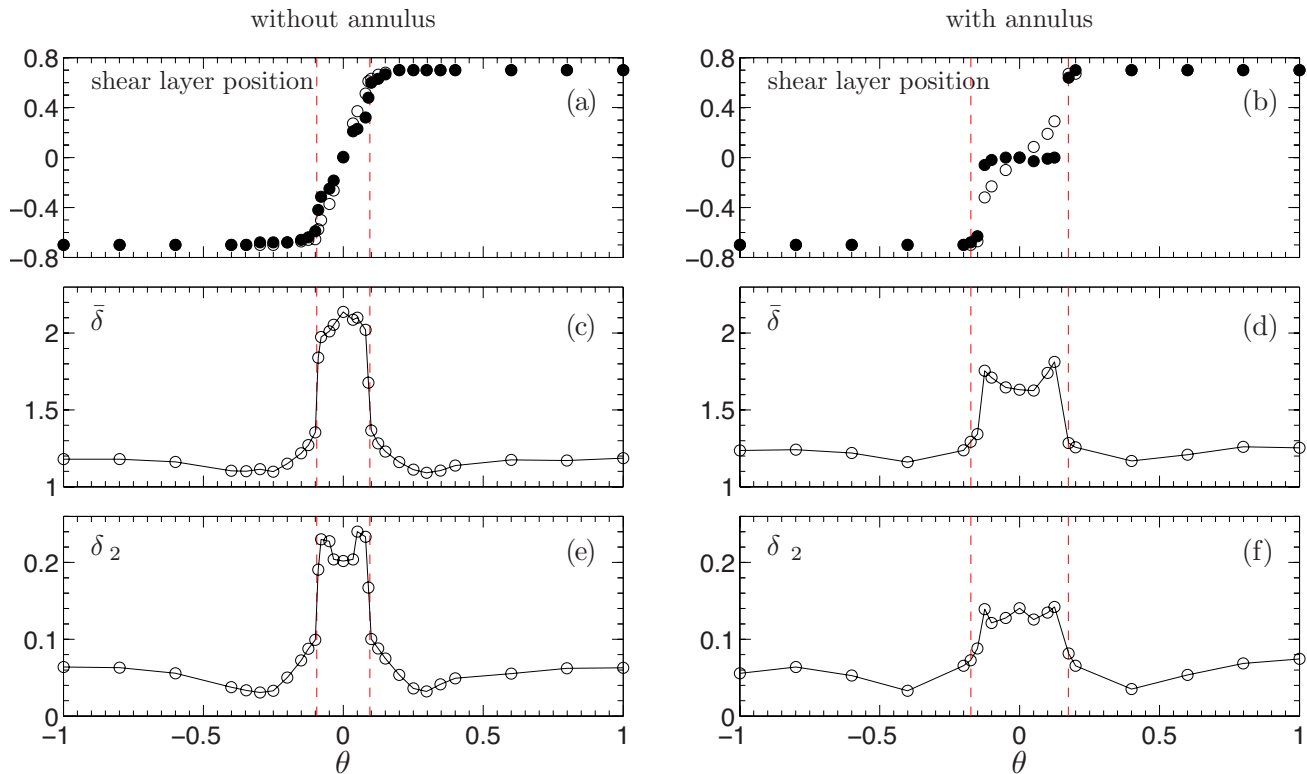


FIG. 9. (Color online) [(a) and (b)] Vertical position of the shear layer at $r=0$ on the rotation axis (\circ) and at position $r=0.7$ (\bullet), [(c) and (d)] $\bar{\delta}$, and [(e) and (f)] δ_2 as a function of the rotation number θ . Left and right columns correspond, respectively, to setup TM73(+) without and with annulus. In (a) and (b), the (\circ) markers correspond to the stagnation point vertical position. In (c)–(f), $\bar{\delta}$ and δ_2 are computed over the whole flow.

C. Properties of δ when $f_1 \neq f_2$

As already mentioned in Sec. III A 3, depending on the value of the rotation number $\theta = (f_1 - f_2) / (f_1 + f_2)$, the mean von Kármán flow exhibits two different topologies. Indeed, for $|\theta| < \theta_c$, the mean flow is composed of two toric recirculation cells separated by an azimuthal shear layer, as for $|\theta| > \theta_c$, it is composed of a single recirculation cell.¹⁸ We have performed a set of experiments for the specific forcing condition TM73(+) with and without annulus, varying θ from -1 to 1 . In this geometry, $\theta_c = 0.17 \pm 0.01$ with annulus and $\theta_c = 0.095 \pm 0.005$ without annulus. The aim of these experiments is to study the influence of the global rotation and of the transition between the two flow topologies on turbulence intensity.

A way to quantify precisely the turbulent bifurcation of the mean flow occurring at θ_c is to study the position of the azimuthal shear layer that separates the recirculation cells when $|\theta| < \theta_c$. A good quantity that allows to localize this position is the zero isosurface of the stream function $\psi(r, z)$ of the mean flow defined through $(\bar{u}_r, 0, \bar{u}_z) = \nabla \times (r^{-1} \bar{\psi} \mathbf{e}_\theta)$ in cylindrical coordinates. Thus, in Figs. 9(a) and 9(b), we have plotted two measures of the shear layer vertical position at $r=0$, i.e., the stagnation point, and at $r=0.7$ on the side. The discrepancies between these two sets of data renders the fact the shear layer is in general a curved surface expect for the $\theta=0$ configuration. Actually, its vertical position at large r is always closer to the $z=0$ equatorial plane of the vessel than at $r=0$. As $|\theta|$ increases from zero, the shear layer is attracted by the slowest impeller. Without annulus [cf. Fig. 9(a)], it

results in a global drift of the shear layer³⁴ accompanied by the appearance of a moderate curvature. With annulus [cf. Fig. 9(b)], the outer edge of the shear layer remains pinned on the annulus whereas its center—the stagnation point—drifts, increasing the layer curvature up to a high level just below θ_c : the annulus strongly stabilizes the shear layer near the equatorial plane and maintains it to higher rotation numbers.

At $\theta = \theta_c$, we observe a discontinuity of the shear layer vertical position which corresponds to the turbulent bifurcation. The discontinuous bifurcation does not present, in the two studied cases, any hysteresis in θ . However, close to θ_c , we can observe transitions between two metastable one cell and two cells states which follow a slow dynamics.³⁵

In this section, we first analyze how the parameters $\bar{\delta}$ and δ_2 behave with the rotation number. Thereafter, using these tools computed over the two symmetric half of the flow, we analyze how they can also provide a proper characterization of the symmetry breaking.

1. Variation of $\bar{\delta}$ with the rotation number

The parameter δ can be used to study the changes in turbulence intensity related to the turbulent bifurcation undertaken by von Kármán flows at critical θ_c . Figures 9(c)–9(f) show the variations of $\bar{\delta}$ and δ_2 , calculated over the whole flow as a function θ .

First of all, for $|\theta| < \theta_c$, $\bar{\delta}$ and δ_2 are relatively high ($\bar{\delta} \approx 2$ and $\delta_2 \approx 0.2$). This reflects the presence of the highly

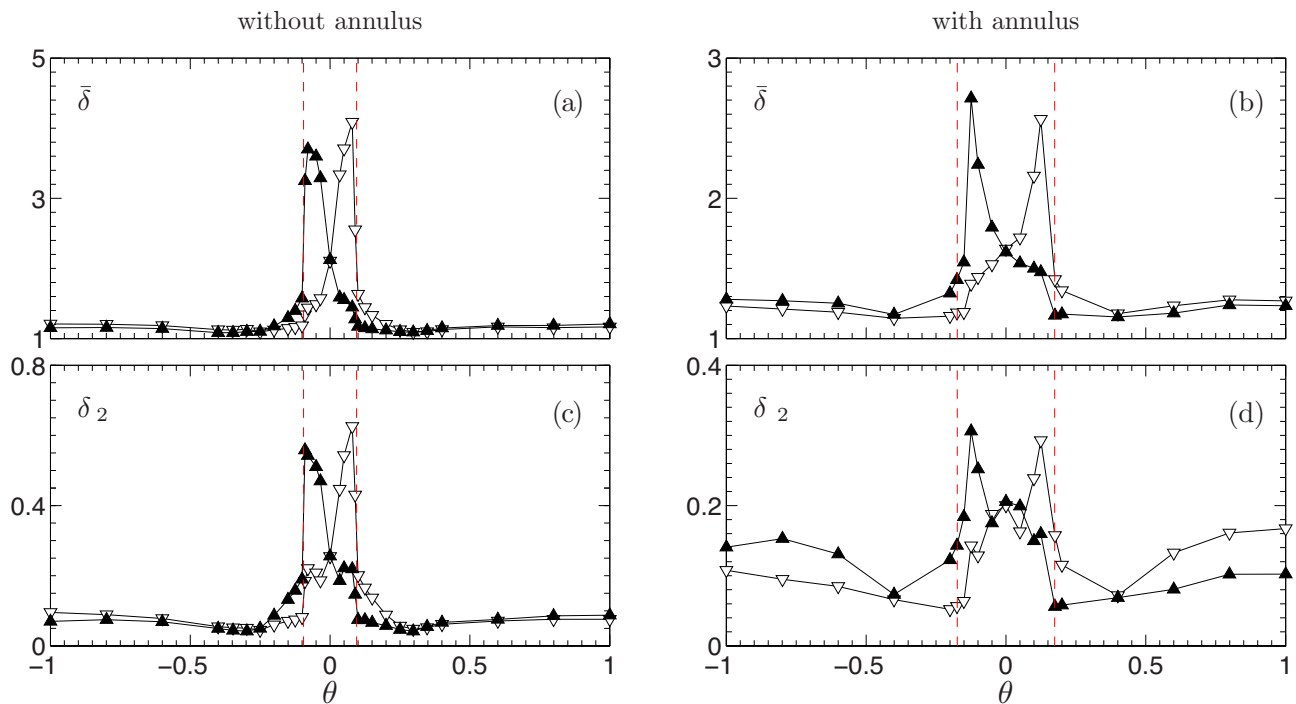


FIG. 10. (Color online) [(a) and (b)] $\bar{\delta}$, and [(c) and (d)] δ_2 , as a function of the rotation number θ . Left and right columns correspond, respectively, to setup TM73(+) without and with annulus. (\blacktriangle) corresponds to δ computed over the upper half part of the flow as (∇) to the lower half part.

fluctuating shear layer in the flow bulk. On the contrary, for $|\theta| > \theta_c$, i.e., for a large rotation-to-shear rate, $\bar{\delta}$ and δ_2 are quite small ($\bar{\delta} \approx 1.2$ and $\delta_2 \approx 0.05$) and are almost independent of θ .³⁶ This means that the level of global rotation has no significant influence on the turbulence intensity level unless the mean flow topology changes. Actually, $\bar{\delta}$ and δ_2 carefully trace back the flow topology changes induced through the bifurcation at $\pm\theta_c$. They might even be used as order parameters of such turbulent bifurcation and they provide a reliable measurement of threshold θ_c .

2. Effect of the annulus

We have seen how the annulus stabilizes the shear layer and postpones the bifurcation threshold. It has also a strong effect on the turbulence level. In Figs. 9(c)–9(f), we observe that for $|\theta| < \theta_c$, when the flow is composed of two counter-rotating toroidal cells, the turbulence level is much larger without than with the annulus: the results for zero rotation number (cf. Sec. IV B) extend to $-\theta_c < \theta < \theta_c$.

We have already mentioned that the strong reduction in $\bar{\delta}$ and δ_2 with the annulus is due to the stabilization and the spatial filtering, especially at large scales, of the shear layer that is trapped by the annulus. Also, we note that the curvature of $\bar{\delta}(\theta)$ is opposite, with and without annulus, in the range $-\theta_c < \theta < \theta_c$. Without annulus, $\bar{\delta}_{w/o}(\theta)$ decreases with increasing $|\theta|$ since the shear layer is free to drift continuously away from $z=0$ as θ tend to $\pm\theta_c^{w/o}$. With the annulus, the shear layer is trapped and we observe that the fluctuation level $\bar{\delta}_w(\theta)$ increases with $|\theta|$ and reaches maxima—and may even diverge—close to $\pm\theta_c'$. Actually, we may suppose that the flow with annulus has a given energy gap to overcome

the trapping of the shear layer and bifurcate from two cells to one cell, i.e., abruptly break the top/bottom symmetry of the flow. This may explain why it is necessary to explore larger θ before turbulent bifurcation occurs, i.e., why θ_c is larger with the annulus than without.

For $|\theta| > \theta_c$, the low turbulence intensity, almost unchanged at first order, is slightly larger in the presence of the annulus: The one-cell flow is almost insensitive to the annulus presence and the slight increase is probably due to the vertical step flow over the annulus.

3. Quantifying the symmetry breaking

For further exploration of the turbulent bifurcation and related symmetry breaking, we now calculate $\bar{\delta}$ and δ_2 over half vessels, i.e., on each side of the annulus equatorial plane (cf. Fig. 10).

Starting from the exact counter-rotating configuration, as $|\theta|$ is increased from zero, $\bar{\delta}$ and δ_2 are becoming larger for the half part of the flow corresponding to the slowest impeller and are decreasing for the other half part. This is directly connected with the position of the shear layer, which gets closer and closer to the slowest impeller when θ increases [cf. Figs. 9(a) and 9(b)].

In Fig. 10, we observe that as it is generally the case in the vicinity of bifurcations, the fluctuation indicators $\bar{\delta}$ and δ_2 grow near $\pm\theta_c$ in the concerned half vessel and that the peaks in $\bar{\delta}$ and δ_2 correspond exactly to the bifurcation points $\theta = \pm\theta_c$. With the annulus, where the bifurcation is much sharper, one could detect a critical divergence for $(\bar{\delta}-1)$ [cf. Fig. 10(b)].

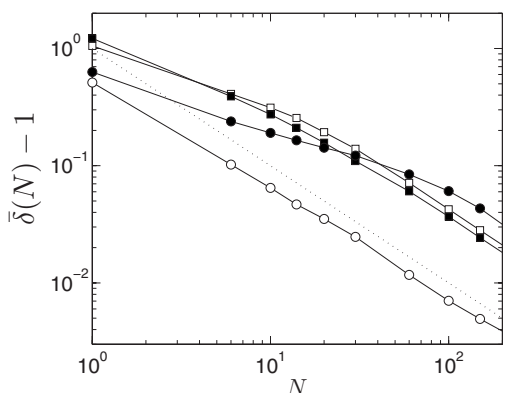


FIG. 11. $\bar{\delta}(N) - 1$ computed with velocity fields averaged over N instantaneous fields for various setups: TM73(-), without the annulus (■) and with the annulus (●) and TM73(+), without annulus (□) and with annulus (○). A guide to the eye for the N^{-1} dependency is plotted with a dotted line.

V. CONCLUSIVE DISCUSSION

We have introduced a hydrodynamical global quantity δ that characterizes turbulent fluctuations in inhomogeneous anisotropic flows. This time dependent quantity is constructed as the ratio of the instantaneous kinetic energy of the flow with the kinetic energy of the time-averaged flow. Such a normalization based on the flow dynamics makes this quantity comparable from one turbulent flow to any other. We have shown that, generally, properties of $\delta(t)$ are fully provided thanks to only two parameters, its time average $\bar{\delta}$ and variance δ_2 . These parameters generalize to inhomogeneous anisotropic flows the classical notion of turbulence intensity, based on local, single point measurements. Additionally, $\bar{\delta}$ and δ_2 present topological and thermodynamical properties since they are connected respectively to the distance between the instantaneous and the time-averaged flow and to the number of degrees of freedom of the flow.

Properties of $\bar{\delta}$ and δ_2 have been experimentally studied in the typical case of the von Kármán flow for different forcing and geometries. We have shown that in the fully turbulent regime, they are Reynolds independent, like any classical quantity in the inertial range. However, $\bar{\delta}$ and δ_2 depend on forcing and geometry and faithfully reflect major changes in the flow topology. They can therefore be used as a tool for comparison of different turbulent flow. In the present paper, we provided an example in which δ is used to characterize the turbulent bifurcation in the von Kármán flow induced through differential rotation of the two impellers. Finally, $\bar{\delta}$ and δ_2 are used to characterize the scale by scale energy budget as a function of the forcing mode as well as the transition between the two flow topologies.

Another interesting application would be the study of the generation of magnetic field by a turbulent flow, the so-called dynamo instability. This problem has attracted recently a lot of experimental attention.^{37–40} In the case where the corresponding turbulent flow has a nonzero mean value, the dynamo instability may be seen as a classical instability problem, governed by the mean flow and the fluctuations.^{24,41,42} A natural question in this case is therefore how to quantify the

relative level of fluctuations, and the deviations from the mean flow they induce, so as to implement efficient control strategies to decrease or increase their influence. Since our global parameter quantify the difference between the instantaneous and the mean flow, they are natural candidate to discriminate between different dynamos. This has been recently illustrated in numerical simulations of the Taylor–Green flow.⁴³ No equivalent quantitative analysis has been performed for experimental dynamos. However, among these successful experimental dynamos, we can suspect that the Riga³⁷ and Karlsruhe³⁸ flows are characterized by values of δ lower than in von Kármán flows.^{39,40} In the future, we plan to use these parameters for the analysis of recent results of the von Kármán sodium (VKS) experiment.

ACKNOWLEDGMENTS

This work was supported by ANR TSF under Grant No. NT05-1-41492.

APPENDIX: CONVERGENCE TOWARD THE MEAN FLOW

As we have seen in Sec. II, the parameter $\bar{\delta}$ can be seen as the average square distance between the instantaneous and the time-averaged velocity fields. Therefore, we can use a slight modification of $\bar{\delta}$ to study the convergence toward the mean flow through statistical averaging. For this, we define $V(N, t)$ the velocity field averaged around time t over N instantaneous fields. $N < N_{\max}$, where $N_{\max} = 5000$ is the total number of instantaneous fields. From a practical point of view, $V(N_{\max}) = \bar{V}(t)$. Then, we define

$$\bar{\delta}(N) = \frac{\langle V^2(N, t) \rangle}{\langle \bar{V}^2 \rangle}. \quad (\text{A1})$$

With this definition, $\bar{\delta}(1) = \bar{\delta}$ and $\bar{\delta}(N_{\max}) = 1$. Moreover, $\bar{\delta}(N) - 1$ measures the average square distance between the partially averaged field $V(N)$ and the mean flow \bar{V} so that its variations with N can be used to study the convergence toward the mean flow. We can see in Fig. 11 that this square distance, $\bar{\delta}(N) - 1$, decreases as N^{-1} , at least at large N , what is typical of an uncorrelated fluctuating quantity. However, for the negative-rotation-sense-with-annulus case, the N^{-1} dependency is observed only at N larger than 100. Actually, in that particular setup, we have observed, by means of bubble seeding (cf. end of Sec. IV B 2), that even if the largest structures of the shear layer were removed by the annulus, a pair of coupled vortices appeared. These vortices are smaller than those we observe without the annulus, but their long time coherent processing must induce long time correlations that slow down the decrease of $\bar{\delta}(N)$.

¹U. Frisch, *Turbulence: The Legacy of A. N. Kolmogorov* (Cambridge University Press, Cambridge, 1995).

²A. Pumir, “Turbulence in homogeneous shear flows,” *Phys. Fluids* **8**, 3112 (1996).

³B. Castaing, Y. Gagne, and E. J. Hopfinger, “Velocity probability density functions of high Reynolds-number turbulence,” *Physica D* **46**, 177 (1990).

- ⁴J. Maurer, P. Tabeling, and G. Zocchi, "Statistics of turbulence between two counterrotating disks in low-temperature helium gas," *Europhys. Lett.* **26**, 31 (1994).
- ⁵S. T. Bramwell, P. C. W. Holdsworth, and J.-F. Pinton, "Universality of rare fluctuations in turbulence and critical phenomena," *Nature (London)* **396**, 552 (1998).
- ⁶J.-F. Pinton, P. C. W. Holdsworth, and R. Labbé, "Power fluctuations in a closed turbulent shear flow," *Phys. Rev. E* **60**, R2452 (1999).
- ⁷J.-H. Titon and O. Cadot, "The statistics of power injected in a closed turbulent flow: Constant torque forcing versus constant velocity forcing," *Phys. Fluids* **15**, 625 (2003).
- ⁸J.-H. Titon and O. Cadot, "Global injected power statistics in a turbulent system: degrees of freedom and aspect ratio effect," *Eur. Phys. J. B* **45**, 289 (2005).
- ⁹R. H. Kraichnan, "Inertial ranges in two-dimensional turbulence," *Phys. Fluids* **10**, 1417 (1967).
- ¹⁰B. Castaing, "The temperature of turbulent flows," *J. Phys. II* **6**, 105 (1996).
- ¹¹S. Ciliberto, N. Garnier, S. Hernandez, C. Lacpatia, J.-F. Pinton, and G. R. Chavarría, "Experimental test of the Gallavotti-Cohen fluctuation theorem in turbulent flows," *Physica A* **340**, 240 (2004).
- ¹²R. Monchaux, P.-P. Cortet, P.-H. Chavanis, A. Chiffaudel, F. Daviaud, P. Diribarne, and B. Dubrulle, "Fluctuation-dissipation relations and statistical temperatures in a turbulent von Kármán flow," *Phys. Rev. Lett.* **101**, 174502 (2008).
- ¹³A. D. Gilbert, "Spiral structures and spectra in two-dimensional turbulence," *J. Fluid Mech.* **193**, 475 (1988).
- ¹⁴J. C. Vassilicos, "Anomalous diffusion of isolated flow singularities and of fractal or spiral structures," *Phys. Rev. E* **52**, R5753 (1995).
- ¹⁵O. Cadot, S. Douady, and Y. Couder, "Characterization of the low-pressure filaments in a three-dimensional turbulent shear flow," *Phys. Fluids* **7**, 630 (1995).
- ¹⁶R. Labbé, J.-F. Pinton, and S. Fauve, "Study of the von Kármán flow between coaxial corotating disks," *Phys. Fluids* **8**, 914 (1996).
- ¹⁷N. Mordant, J.-F. Pinton, and F. Chillà, "Characterization of turbulence in a closed flow," *J. Phys. II* **7**, 1729 (1997).
- ¹⁸F. Ravelet, L. Marié, A. Chiffaudel, and F. Daviaud, "Multistability and memory effect in a highly turbulent flow: Experimental evidence for a global bifurcation," *Phys. Rev. Lett.* **93**, 164501 (2004).
- ¹⁹C. Nore, F. Moisy, and L. Quartier, "Experimental observation of near-heteroclinic cycles in the von Kármán swirling flow," *Phys. Fluids* **17**, 064103 (2005).
- ²⁰P. Tabeling, G. Zocchi, F. Belin, J. Maurer, and H. Willaime, "Probability density functions, skewness, and flatness in large Reynolds number turbulence," *Phys. Rev. E* **53**, 1613 (1996).
- ²¹A. Arneodo, C. Baudet, F. Belin, R. Benzi, B. Castaing, B. Chabaud, R. Chavarría, S. Ciliberto, R. Camussi, F. Chillà, B. Dubrulle, Y. Gagne, B. Hebral, J. Herweijer, M. Marchand, J. Maurer, J.-F. Muzy, A. Naert, A. Noullez, J. Peinke, F. Roux, P. Tabeling, W. van de Water, and H. Willaime, "Structure functions in turbulence, in various flow configurations, at Reynolds number between 30 and 5000, using extended self-similarity," *Europhys. Lett.* **34**, 411 (1996).
- ²²L. Marié, "Transport de moment cinétique et de champ magnétique par un écoulement tourbillonnaire turbulent: Influence de la rotation," Ph.D. thesis, Université Paris VII, 2003.
- ²³L. Marié and F. Daviaud, "Experimental measurement of the scale-by-scale momentum transport budget in a turbulent shear flow," *Phys. Fluids* **16**, 457 (2004).
- ²⁴J.-P. Laval, P. Blaineau, N. Leprovost, B. Dubrulle, and F. Daviaud, "Influence of turbulence on the dynamo threshold," *Phys. Rev. Lett.* **96**, 204503 (2006).
- ²⁵S. Aumaître, J. Farago, S. Fauve, and S. Mc Namara, "Energy and power fluctuations in vibrated granular gases," *Eur. Phys. J. B* **42**, 255 (2004).
- ²⁶S. Aumaître, A. Alastuey, and S. Fauve, "A quasi-elastic regime for vibrated granular gases," *Eur. Phys. J. B* **54**, 263 (2006).
- ²⁷These impellers have been historically designed for efficient dynamo action in the VKS experiment held in CEA-Cadarache. Impellers TM60 were designed, studied (Ref. 44), and tested in a first sodium experimental setup, called VKS1, during years 2000–2002 (Ref. 45). This setup did not succeed in producing dynamo action. Further optimization process led to TM73 impellers design (Refs. 28 and 33) and to a new experimental setup VKS2. In this system, successful dynamo action has been achieved in 2006 (Ref. 39).
- ²⁸F. Ravelet, A. Chiffaudel, F. Daviaud, and J. Leorat, "Toward an experimental von Kármán dynamo: Numerical studies for an optimized design," *Phys. Fluids* **17**, 117104 (2005).
- ²⁹F. Ravelet, A. Chiffaudel, and F. Daviaud, "Supercritical transition to turbulence in an inertially driven von Kármán closed flow," *J. Fluid Mech.* **601**, 339 (2008).
- ³⁰B. Portelli, P. C. W. Holdsworth, and J.-F. Pinton, "Intermittency and non-Gaussian fluctuations of the global energy transfer in fully developed turbulence," *Phys. Rev. Lett.* **90**, 104501 (2003).
- ³¹S. Aumaître, S. Fauve, S. Mc Namara, and P. Poggi, "Power injected in dissipative systems and the fluctuation theorem," *Eur. Phys. J. B* **19**, 449 (2001).
- ³²R. Monchaux, F. Ravelet, B. Dubrulle, A. Chiffaudel, and F. Daviaud, "Properties of steady states in turbulent axisymmetric flows," *Phys. Rev. Lett.* **96**, 124502 (2006).
- ³³R. Monchaux, "Mécanique statistique et effet dynamo dans un écoulement de von Kármán turbulent," Ph.D. thesis, Université Paris VII, 2007.
- ³⁴O. Cadot and O. Le Maître, "The turbulent flow between two rotating stirrers: similarity laws and transitions for the driving torques fluctuations," *Eur. J. Mech. B/Fluids* **26**, 258 (2007).
- ³⁵Careful analysis of the critical regimes by torque measurements, to be reported elsewhere, has been performed with the annulus. In a very narrow range $0.171 \approx \theta \approx 0.179$, we observe very slow dynamical regimes where the topology changes back and forth along time over hours. This explains why, very close to θ_c , some of the present measurements—acquired for only 10 min—may not appear to be of the expected topology in Fig. 9.
- ³⁶If regions of high level of turbulence due to shear still exist, they should be confined inside the blades of the slow rotating impeller, where measurements are impossible to carry on.
- ³⁷A. Gailitis, O. Lielausis, E. Platācis, S. Dement'ev, A. Cifersons, G. Gerbeth, T. Gundrum, F. Stefani, M. Christen, and G. Will, "Magnetic field saturation in the Riga dynamo experiment," *Phys. Rev. Lett.* **86**, 3024 (2001).
- ³⁸R. Stieglitz and U. Müller, "Experimental demonstration of a homogeneous two-scale dynamo," *Phys. Fluids* **13**, 561 (2001).
- ³⁹R. Monchaux, M. Berhanu, M. Bourgoin, M. Moulin, Ph. Odier, J.-F. Pinton, R. Volk, S. Fauve, N. Mordant, F. Pétrélis, A. Chiffaudel, F. Daviaud, B. Dubrulle, C. Gasquet, L. Marié, and F. Ravelet, "Generation of magnetic field by dynamo action in a turbulent flow of liquid sodium," *Phys. Rev. Lett.* **98**, 044502 (2007).
- ⁴⁰M. Berhanu, R. Monchaux, S. Fauve, N. Mordant, F. Petrelis, A. Chiffaudel, F. Daviaud, B. Dubrulle, L. Marie, F. Ravelet, M. Bourgoin, Ph. Odier, J.-F. Pinton, and R. Volk, "Magnetic field reversals in an experimental turbulent dynamo," *Europhys. Lett.* **77**, 59001 (2007).
- ⁴¹N. Leprovost and B. Dubrulle, "The turbulent dynamo as an instability in a noisy medium," *Eur. Phys. J. B* **44**, 395 (2005).
- ⁴²F. Pétrélis and S. Fauve, "Inhibition of the dynamo effect by phase fluctuations," *Europhys. Lett.* **76**, 602 (2006).
- ⁴³B. Dubrulle, P. Blaineau, O. Mafra Lopes, F. Daviaud, J.-P. Laval, and R. Dolganov, "Bifurcations and dynamo action in a Taylor-Green flow," *New J. Phys.* **9**, 308 (2007).
- ⁴⁴L. Marié, J. Burguete, F. Daviaud, and J. Leorat, "Numerical study of homogeneous dynamo based on experimental von Kármán type flows," *Eur. Phys. J. B* **33**, 469 (2003).
- ⁴⁵M. Bourgoin, L. Marié, F. Pétrélis, C. Gasquet, A. Guigon, J.-B. Luciani, M. Moulin, F. Namer, J. Burguete, A. Chiffaudel, F. Daviaud, S. Fauve, P. Odier, and J.-F. Pinton, "MHD measurements in the von Kármán sodium experiment," *Phys. Fluids* **14**, 3046 (2002).